

# Two- and three-dimensional wide-field weak lensing mass maps from the Hyper Suprime-Cam Subaru Strategic Program S16A data

Masamune OGURI<sup>1,2,3</sup>, Satoshi MIYAZAKI<sup>4,5</sup>, Chiaki HIKAGE<sup>3</sup>,  
Rachel MANDELBAUM<sup>6</sup>, Yousuke UTSUMI<sup>7</sup>, Hironao MIYATAKE<sup>8,3</sup>,  
Masahiro TAKADA<sup>3</sup>, Robert ARMSTRONG<sup>9</sup>, James BOSCH<sup>9</sup>,  
Yutaka KOMIYAMA<sup>4,5</sup>, Alexie LEAUTHAUD<sup>10</sup>, Surhud MORE<sup>3</sup>,  
Atsushi J. NISHIZAWA<sup>11</sup>, Nobuhiro OKABE<sup>7,12,13</sup> and Masayuki TANAKA<sup>4</sup>

<sup>1</sup>Research Center for the Early Universe, University of Tokyo, Tokyo 113-0033, Japan

<sup>2</sup>Department of Physics, University of Tokyo, Tokyo 113-0033, Japan

<sup>3</sup>Kavli Institute for the Physics and Mathematics of the Universe (Kavli IPMU, WPI), University of Tokyo, Chiba 277-8582, Japan

<sup>4</sup>National Astronomical Observatory of Japan, Mitaka, Tokyo 181-8588, Japan

<sup>5</sup>Department of Astronomy, School of Science, Graduate University for Advanced Studies, Mitaka, Tokyo 181-8588, Japan

<sup>6</sup>McWilliams Center for Cosmology, Department of Physics, Carnegie Mellon University, Pittsburgh, PA 15213, USA

<sup>7</sup>Hiroshima Astrophysical Science Center, Hiroshima University, Higashi-Hiroshima, Kagamiyama 1-3-1, 739-8526, Japan

<sup>8</sup>Jet Propulsion Laboratory, California Institute of Technology, Pasadena, CA 91109, USA

<sup>9</sup>Department of Astrophysical Sciences, Princeton University, 4 Ivy Lane, Princeton, NJ 08544, USA

<sup>10</sup>Department of Astronomy and Astrophysics, University of California, Santa Cruz, 1156 High Street, Santa Cruz, CA 95064, USA

<sup>11</sup>Institute for Advanced Research, Nagoya University, Nagoya 464-8602, Aichi, Japan

<sup>12</sup>Department of Physical Science, Hiroshima University, 1-3-1 Kagamiyama, Higashi-Hiroshima, Hiroshima 739-8526, Japan

<sup>13</sup>Core Research for Energetic Universe, Hiroshima University, 1-3-1, Kagamiyama, Higashi-Hiroshima, Hiroshima 739-8526, Japan

\*E-mail: masamune.oguri@ipmu.jp

Received ; Accepted

## Abstract

We present wide-field ( $167 \text{ deg}^2$ ) weak lensing mass maps from the Hyper Supreme-Cam Subaru Strategic Program (HSC-SSP). We compare these weak lensing based dark matter maps with maps of the distribution of the stellar mass associated with luminous red galaxies. We find a strong correlation between these two maps with a correlation coefficient of  $\rho = 0.54 \pm 0.03$  (for a smoothing size of  $8'$ ). This correlation is detected even with a smaller smoothing scale of  $2'$  ( $\rho = 0.34 \pm 0.01$ ). This detection is made uniquely possible because of the high source density of the HSC-SSP weak lensing survey ( $\bar{n} \sim 25 \text{ arcmin}^{-2}$ ). We also present

a variety of tests to demonstrate that our maps are not significantly affected by systematic effects. By using the photometric redshift information associated with source galaxies, we reconstruct a three-dimensional mass map. This three-dimensional mass map is also found to correlate with the three-dimensional galaxy mass map. Cross-correlation tests presented in this paper demonstrate that the HSC-SSP weak lensing mass maps are ready for further science analyses.

**Key words:** dark matter — gravitational lensing: weak — large-scale structure of universe

## 1 Introduction

Weak gravitational lensing has developed into a useful probe of the Universe. Weak gravitational lensing takes advantage of small distortions (“shears”) of distant galaxies which are caused by the deflection of light ray paths by intervening gravitational fields, as predicted by General Relativity. While the matter component of the Universe is dominated by dark matter which cannot directly be seen, weak gravitational lensing allows us to directly map out the total mass distribution including dark matter.

Many weak lensing studies focus on two-point statistics of the shear, which is a direct observable of weak lensing analyses, such as cosmic shear and tangential shear around galaxies and clusters of galaxies (e.g., Bartelmann & Schneider 2001; Hoekstra & Jain 2008). However, one can also directly reconstruct the projected mass distribution from the observed shear map (e.g., Kaiser & Squires 1993; Seitz & Schneider 1995; Schneider 1996). Such weak lensing mass maps provide an important means of studying the large-scale structure of the Universe as well as non-Gaussian features of the matter density field. For example, massive clusters of galaxies can be identified from peaks in mass maps (e.g., Miyazaki et al. 2002, 2007; Wittman et al. 2006; Shan et al. 2012; Utsumi et al. 2014; Liu et al. 2015). Correlations of mass maps with light maps constructed from galaxies and clusters of galaxies can reveal the connection between mass and light, by constraining mass-to-light ratios and galaxy biases (e.g., Hoekstra et al. 2002; Okabe et al. 2010; Jullo et al. 2012; Chang et al. 2016; Pujol et al. 2016; Utsumi et al. 2016). These applications of mass maps may be enhanced further by interpolation methods to recover mass maps in masked regions (e.g., Pires et al. 2009; VanderPlas et al. 2012).

Weak lensing mass maps have been constructed in many surveys, including the Cosmological Evolution Survey (COSMOS; Massey et al. 2007), Deep Lens Survey (DLS; Kubo et al. 2009), the Canada-France-Hawaii Telescope Lensing Survey (CFHTLenS; Van Waerbeke et al. 2013), the CFHT/MegaCam Stripe-82 Survey (CS82; Shan et al. 2014), Dark Energy Survey Science Verification data (DES SV; Chang et al. 2015; Vikram et al. 2015), the Kilo-Degree Survey (KiDS; Kuijken et al. 2015), and the Red Cluster Sequence Lensing Survey

(RCSLenS; Hildebrandt et al. 2016). It has been shown that these mass maps correlate well with the light distributions estimated from galaxies, which demonstrated the power of weak lensing measurements for these surveys. These mass maps have also been used to check residual systematics, by cross-correlating them with any parameters related to Point Spread Function (PSF) and observing conditions, as residual systematics in weak lensing measurements can produce apparent correlations with these parameters.

While weak gravitational lensing for a fixed source redshift can only probe the two-dimensional matter density field projected along the line-of-sight, one can reconstruct the three-dimensional mass distribution as well by combining weak lensing mass reconstructions in different source redshift bins (e.g., Taylor 2001; Hu & Keeton 2002; Bacon & Taylor 2003; Simon et al. 2009; VanderPlas et al. 2011; Leonard et al. 2014; Böhm et al. 2017). The idea has been applied to observations to obtain three-dimensional mass maps (Taylor et al. 2004; Massey et al. 2007; Simon et al. 2012), although they have been restricted to relatively small areas given the requirement of high source galaxy densities. One can improve the accuracy of three-dimensional mass reconstructions by using some information from galaxy distributions as a prior (e.g., Amara et al. 2012; Szepletowski et al. 2014), although with this approach the resulting mass maps are no longer independent of galaxy light distributions.

In this paper, we present two-dimensional and three-dimensional mass maps from the Hyper Suprime-Cam (HSC) Subaru Strategic Program (Aihara et al. 2017a, 2017b), a wide-field imaging survey using the Hyper Suprime-Cam (Miyazaki et al. 2017a) mounted on the Subaru 8.2-meter telescope. Weak lensing analysis of commissioning data has already demonstrated that the HSC is a powerful instrument for weak lensing studies (Miyazaki et al. 2015; Utsumi et al. 2016). The purpose of this paper is to construct weak lensing mass maps to check the performance of weak lensing measurements in the HSC survey. To do so, we cross-correlate weak lensing mass maps with the distribution of stellar masses of red galaxies, which are known to trace the large-scale structure of the Universe. We also cross-correlate our mass maps with maps of various quantities such as PSF and seeing sizes, to check for any possible residual

systematics in the reconstructed mass maps. Validating mass maps is important for future applications of weak lensing mass maps in the HSC survey, including the construction of mass-selected cluster samples and cross-correlations of weak lensing maps with other surveys such as ACTPol.

This paper is organized as follows. In Section 2, we describe our source galaxy catalog for weak lensing analysis as well as our photometric red galaxy sample used for constructing galaxy mass maps. Our two-dimensional mass map analysis is presented in Section 3, whereas our three-dimensional mass map analysis is presented in Section 4. We summarize our result in Section 5. Unless otherwise specified, we assume a flat  $\Lambda$ -dominated cosmology with the matter density  $\Omega_M = 0.27$ , the baryon density  $\Omega_b = 0.045$ , cosmological constant  $\Omega_\Lambda = 0.73$ , dimensionless Hubble constant  $h = 0.71$ , the power spectrum tilt  $n_s = 0.96$ , and the normalization of the density fluctuation  $\sigma_8 = 0.80$ . We note that our conclusion is insensitive to the choice of the cosmological parameters.

## 2 Data

### 2.1 Weak lensing shear catalog

Galaxy shape measurements and the resulting shear catalog in the HSC S16A dataset are detailed in Mandelbaum et al. (2017). In short, the shapes of galaxies in the coadded  $i$ -band images are estimated using the re-Gaussianization method (Hirata & Seljak 2003), and are calibrated using simulated galaxy images that are similar to those used in GREAT3 (Mandelbaum et al. 2015). The image simulation includes realistic HSC PSFs and is carefully designed to reproduce the observed distribution of galaxy properties remarkably well, which allows a reliable estimate shear calibration and additive biases (see Mandelbaum et al., in prep.). We use conservative cuts for selecting galaxies with secure shape measurements, e.g.,  $S/N \geq 10$  and  $i \leq 24.5$ . The shear catalog has been tested and shown to pass requirements for cosmological studies. The shape catalog contains  $\sim 12$  million galaxies selected from  $137 \text{ deg}^2$ , giving an average raw number density of galaxies  $\bar{n} \sim 25 \text{ arcmin}^{-2}$ .

The HSC S16A dataset consists (mostly) of 6 patches; XMM, GAMA09H, GAMA15H, HECTOMAP, VVDS, and WIDE12H. While we present mass maps for these individual patches separately, we combine our results on cross-correlations for all these 6 patches.

Accurate photometric redshifts for the shape catalog are important, particularly for three-dimensional weak lensing mass reconstructions. Thus we apply an additional cut to select galaxies with secure photometric redshifts. We do so by selecting galaxies with the standard deviation computed from the probability distribution function (PDF) of the photometric redshift smaller than 0.3. This cut removes  $\sim 16\%$  of the galaxies from the shape catalog. While photometric redshifts are measured for

the HSC galaxies using several different techniques, throughout this paper we use the `m1z` photometric redshifts (Tanaka et al. 2017).

We use mock shear catalogs to estimate statistical uncertainties on the mass maps. Details of the mock shear catalogs are given in Appendix 1.

### 2.2 Galaxy catalog

We need a galaxy sample with reasonably accurate redshift information in order to compare mass maps from weak lensing with galaxy distributions. While the HSC survey footprint overlaps SDSS, the redshift coverage of SDSS spectroscopic galaxies is limited. Following redMaGiC (Roza et al. 2016), in this paper we construct a photometrically selected sample of luminous red galaxies (LRGs) from the HSC data by taking advantage of the Stellar Population Synthesis (SPS) fitting method developed for the CAMIRA algorithm (Oguri 2014; Oguri et al. 2017). The CAMIRA algorithm fits all galaxies with the SPS model of passively evolving galaxies from Bruzual & Charlot (2003), with careful corrections for slight color differences between the model and observations using spectroscopic galaxies, to compute the goodness-of-fit  $\chi^2$  which is used to construct a three-dimensional richness map for identifying clusters of galaxies. The calibration for the HSC survey and the resulting cluster catalog is presented in Oguri et al. (2017), in which  $\sim 2000$  clusters of galaxies at  $0.1 < z < 1.1$  selected from the area of  $\sim 230 \text{ deg}^2$  are reported.

We use this SPS model calibrated in the HSC survey (see Oguri et al. 2017) to select LRGs as follows. We fit all galaxies with the SPS model, leaving redshift, stellar mass, and metallicity as model parameters. In this model a single instantaneous burst at the formation redshift  $z_f = 3$  is assumed, and a prior is added to the metallicity (see Oguri 2014). Since we only consider passively evolving galaxies in the SPS model, any galaxies that can be fit well with the SPS model are red galaxies. Specifically, we select galaxies with best-fit  $\chi^2 < 10$  (3 degrees of freedom). In order to construct a roughly volume-limited galaxy sample, we restrict the redshift range to  $0.05 < z_{\text{photo}} < 1.05$ , where  $z_{\text{photo}}$  is the best-fit photometric redshift, and the stellar mass range to  $M_* > 10^{10.3} M_\odot$ , where the stellar mass is derived assuming the Salpeter (1955) initial mass function. From the HSC S16A Wide dataset, we select 1,024,729 LRGs that satisfy these criteria.

We cross match the LRGs with spectroscopic galaxies in the HSC footprint (see Oguri et al. 2017, and references therein) to check the accuracy of the photometric redshifts of LRGs. Using 51,402 LRGs that match the spectroscopic galaxy catalog, we derive the scatter  $\sigma_z$  and bias  $\delta_z$  of the residual  $(z_{\text{LRG}} - z_{\text{spec}})/(1 + z_{\text{spec}})$ . Figure 1 shows the scatter and bias as a function of redshift. Here we apply  $3\sigma$  clipping when esti-

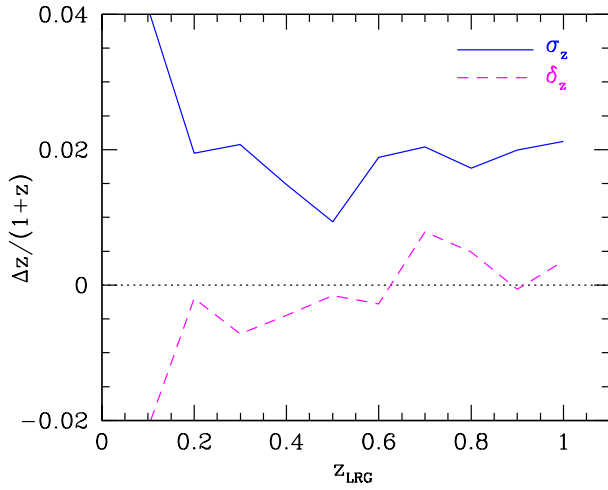


**Fig. 1.** Comparison of photometric redshifts of LRGs  $z_{\text{LRG}}$  with their spectroscopic redshifts  $z_{\text{spec}}$ . We plot the scatter  $\sigma_z$  (solid) and bias  $\delta_z$  (dashed) of the residual  $(z_{\text{LRG}} - z_{\text{spec}})/(1 + z_{\text{spec}})$  as a function of redshift.

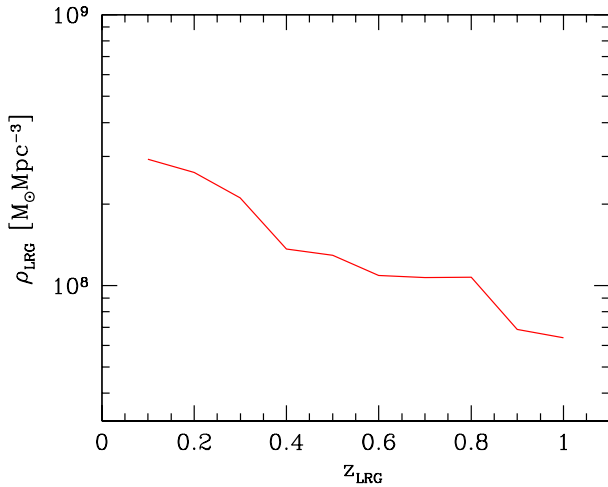


**Fig. 2.** Stellar mass densities of LRGs  $\rho_{\text{LRG}}$  as a function of photometric redshift, for LRGs with stellar masses  $M_* > 10^{10.3} M_\odot$ .

inating the scatter and bias. The resulting outlier rate is  $\sim 7\%$  for the whole sample. We find that the scatter is  $\sigma_z \sim 0.02$  for the whole redshift range of interest, except for the lowest redshift  $z \sim 0.1$  which is probably due to relatively poor photometric accuracy of nearby, very bright galaxies in the HSC survey. The relatively poor photometric redshifts at the lowest redshift may also be due to the lack of  $u$ -band images. We also note that the scatter is larger than the scatter of photometric redshifts of CAMIRA clusters,  $\sigma_z \lesssim 0.01$ , because the cluster photometric redshifts are derived by combining photometric redshifts of several cluster member galaxies.

In Figure 2, we derive the stellar mass density of LRGs by summing up the stellar masses of all the LRGs with  $M_* > 10^{10.3} M_\odot$ . The stellar mass density increases from  $z = 1$  to 0, which is broadly consistent with previous analysis of the evolution of early-type galaxies (e.g., Bell et al. 2004).

### 3 Two-dimensional mass maps

#### 3.1 Mass reconstruction technique

The construction of mass maps from weak lensing requires spatial filtering to reduce noise. There are several possible choices of spatial filters which must be chosen depending on the application of the mass maps. Miyazaki et al. (2017b) also constructs wide-field mass maps from the same HSC data, but they are interested in identifying clusters of galaxies from peaks in mass maps. In searching for clusters, it is beneficial to use spatial filters that eliminate the large-scale power in order to reduce the scatter in peak heights coming from the large-scale structure. In contrast, since we are interested in the large-scale structure, in this paper we use a Gaussian filter which retains the large-scale power. Systematic tests with  $B$ -mode mass maps are also presented in Mandelbaum et al. (2017) and Miyazaki et al. (2017b).

In this paper we follow a mass reconstruction method proposed by Kaiser & Squires (1993). Since we are interested in large-scale mass distributions, in this paper we always consider the weak lensing limit,  $|\kappa| \ll 1$ . First we smooth the shear field  $\gamma_\alpha(\theta)$  ( $\alpha = 1, 2$ ) as (Seitz & Schneider 1995)

$$\hat{\gamma}_\alpha(\theta) = \frac{\sum_i w_i [\gamma_\alpha(\theta_i) - c_{\alpha,i}] W(|\theta - \theta_i|)}{\sum_i w_i (1 + m_i) W(|\theta - \theta_i|)}, \quad (1)$$

where  $w_i$  is the inverse variance weight for the  $i$ -th galaxy given in the weak lensing shear catalog, the shear  $\gamma_\alpha(\theta_i)$  is related to the distortion  $e_\alpha$  (the ellipticity defined by second moments of the galaxy image) as  $\gamma_\alpha(\theta_i) = e_\alpha(\theta_i)/2\mathcal{R}$  with  $\mathcal{R}$  being the shear responsivity that connects the distortion and the shear,  $W(\theta)$  is the Gaussian smoothing kernel

$$W(\theta) = \frac{1}{\pi\theta_s^2} \exp\left(-\frac{\theta^2}{\theta_s^2}\right), \quad (2)$$

and  $m_i$  and  $c_{\alpha,i}$  are the multiplicative and additive biases for the  $i$ -th galaxy (see Mandelbaum et al. 2017 for more details on the shear responsivity and calibration factors). We then convert the shear field to the convergence field via

$$\hat{\kappa}(\theta) = \frac{1}{\pi} \int d^2\theta' \frac{\hat{\gamma}_t(\theta'|\theta)}{|\theta - \theta'|^2}, \quad (3)$$

where  $\gamma_t(\theta'|\theta)$  is a tangential shear at position  $\theta'$  computed with respect to the reference position  $\theta$ .

In practice we construct the mass map on a regular grid adopting a flat-sky approximation. First, we create a pixelized shear map for each of the 6 patches with a pixel size of  $0'.5$ , apply the Fast Fourier Transform (FFT), and conduct the convolutions in the Fourier space to obtain the smoothed convergence map, which is sometimes referred as an  $E$ -mode mass map. Since FFT assumes a periodic boundary condition, we apply zero padding beyond the boundary of the image before FFT. The imaginary part of the reconstructed convergence map represents a  $B$ -mode mass map, which is used to check for certain types of residual systematics in our weak lensing measurements. In Mandelbaum et al. (2017), we show that the  $B$ -mode

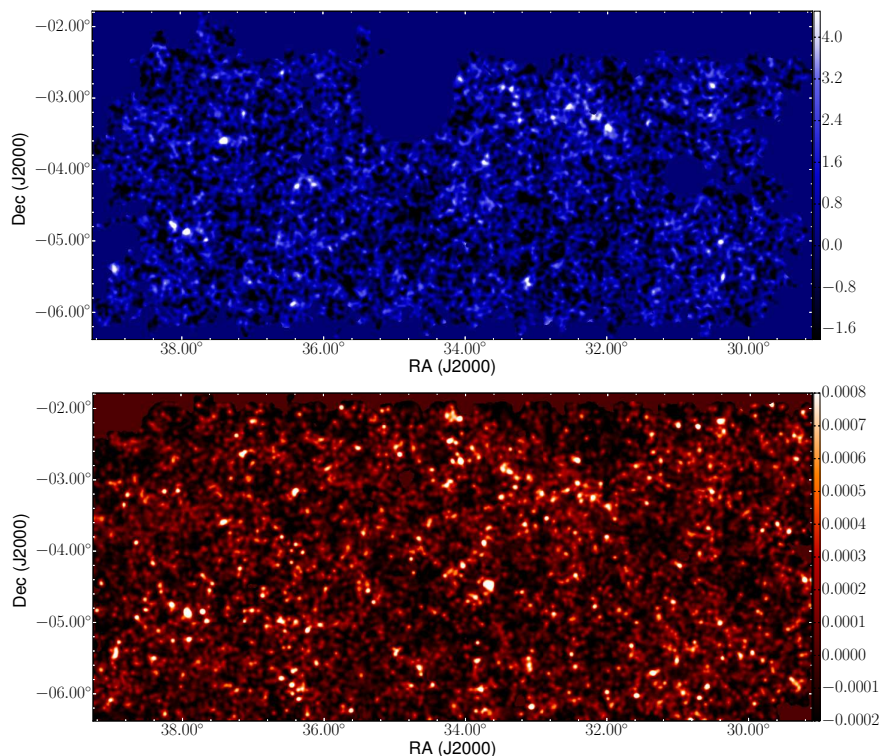


**Fig. 3.** Total mass (*upper*) and galaxy mass (*lower*) maps in the XMM field. In the total mass map, we show the S/N of the weak lensing reconstructed map, which is roughly proportional to the convergence  $\kappa$ . In the galaxy mass map we directly show the galaxy mass map value  $\kappa_g$  defined in equation (4). The smoothing scale is  $\theta_s = 2'$  (see equation 2).

mass map PDF well follows the Gaussian distribution as expected for weak lensing mass maps without significant systematic errors in shape measurements. In fact, the boundary effect induces small non-vanishing  $B$ -mode signals, which can be estimated from our mock shape catalog which has exactly the same geometry as our input HSC shape catalog (see also Mandelbaum et al. 2017).

We also construct a noise map as follows. We randomly rotate the orientations of individual galaxies, and construct a mass map using the randomized galaxy catalog. We repeat this procedure to create 300 random mass maps from 300 realizations of randomized galaxy catalogs. We then compute a standard deviation of each pixel from the 300 random mass maps to construct a “sigma map”, a map showing the spatial variation of the statistical noise of the reconstructed mass map. The sigma map includes only the shape noise and measurement error, and does not include cosmic shear. From the sigma map we can define the signal-to-noise ratio (S/N) for each pixel simply from the ratio of the  $\kappa$  value of the reconstructed mass map to the standard deviation of  $\kappa$  from the sigma map.

In real observations, there are several regions where data are missing due to bright star masks and edges. Reconstructed mass maps in and near those regions are noisy and are not suitable for analysis. To determine the mask region for each mass map, we construct a number density map of the input galaxy catalog

by convolving the number density in each pixel with the same smoothing kernel which was used in constructing mass maps (equation 2). Then we derive the mean of the number density map with  $2.5\sigma$  clipping. We adopt clipping because the number density map has a non-Gaussian tail. We mask all pixels with the *smoothed* number density less than 0.5 times the mean number density computed above, assuming that they correspond to edges and regions that are affected by bright star masks. In addition, we derive the mean of the sigma map with  $2.5\sigma$  clipping and mask all pixels with the noise value larger than twice the mean value, although this additional cut removes only a minor fraction of the survey area. The criteria for these masking procedures are determined empirically so that the degradation of the mass map at the edge is not significant.

We show the mass maps of the 6 HSC S16A patches in Figures 3, 4, 5, 6, 7, and 8. These mass maps are created using a relatively small smoothing scale of  $\theta_s = 2'$ . Here we show S/N maps which are similar to  $\kappa$  maps except near the edges where the noise is slightly larger. In the cross-correlation analysis below we use  $\kappa$  maps rather than S/N maps. The total area of unmasked regions in these mass maps is  $\sim 167 \text{ deg}^2$ , which is larger than the total area of the regions where the weak lensing shape catalog is defined,  $\sim 137 \text{ deg}^2$  (see Mandelbaum et al. 2017), because of the non-local nature of the weak lensing mass reconstruction.

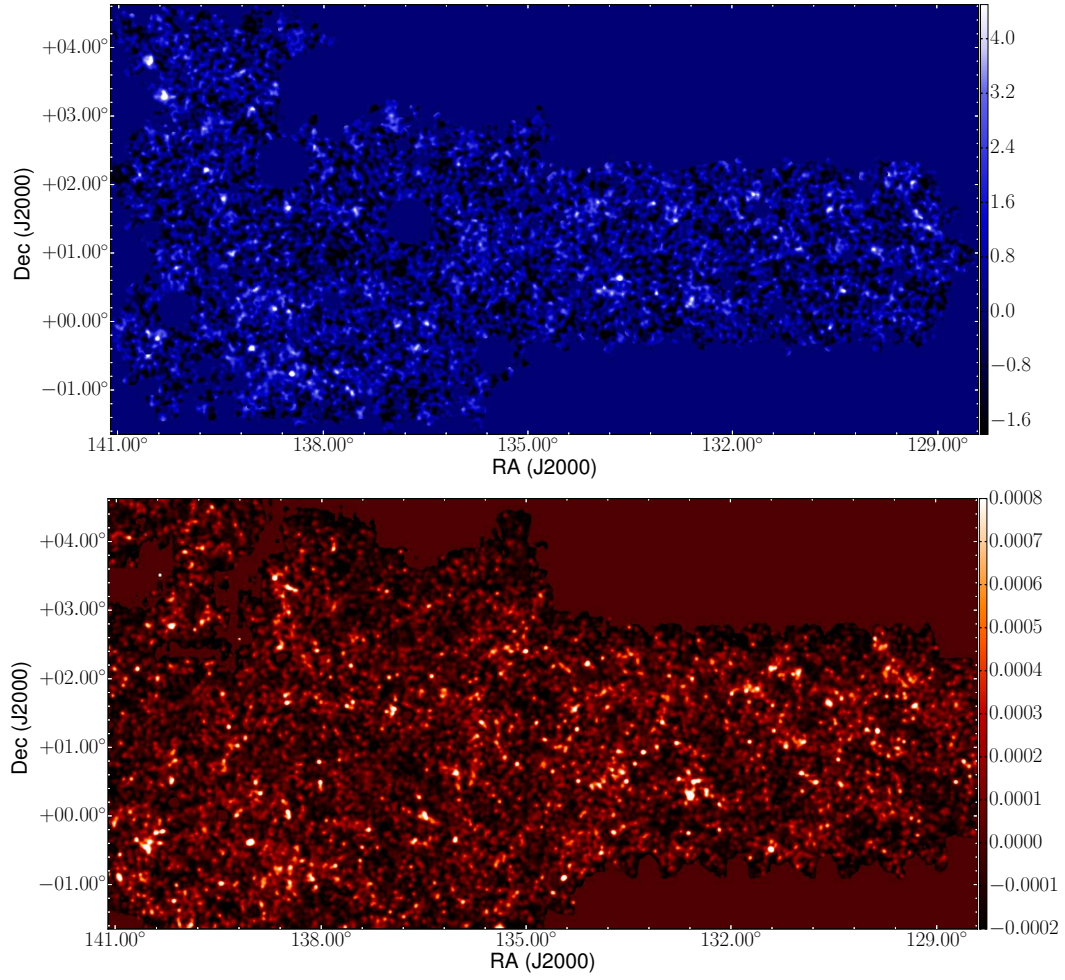


Fig. 4. Same as Figure 3, but for the GAMA09H field.

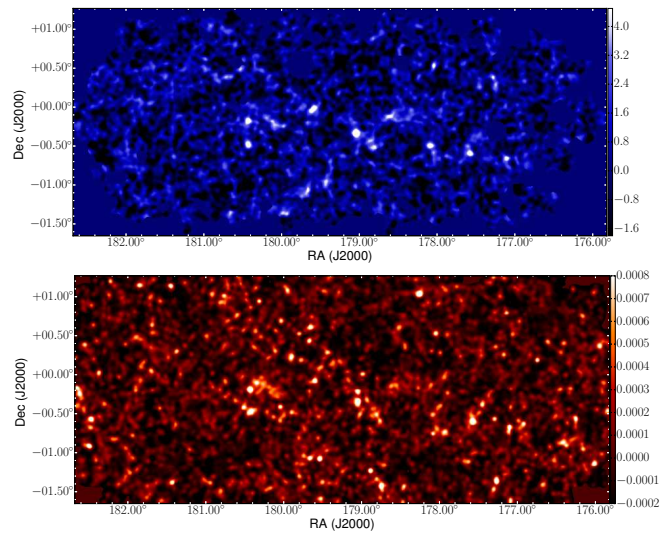


Fig. 5. Same as Figure 3, but for the WIDE12H field.

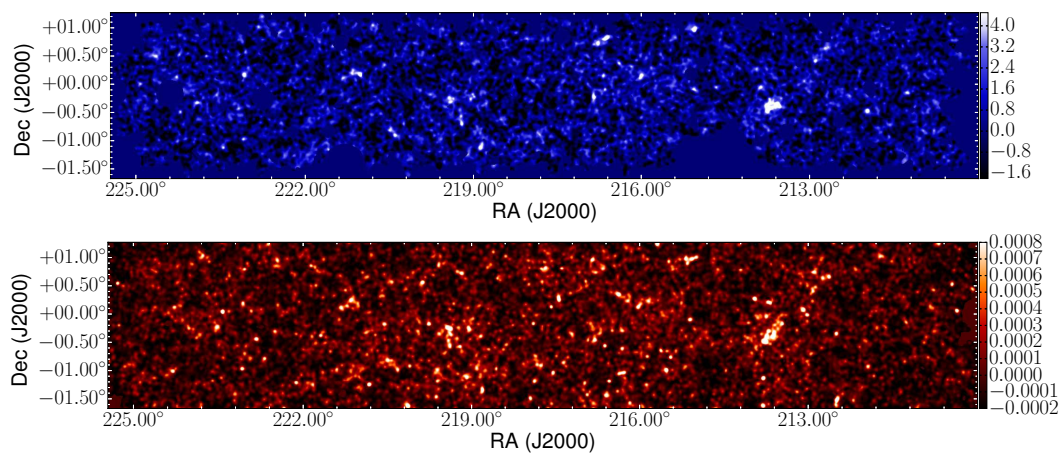


Fig. 6. Same as Figure 3, but for the GAMA15H field.

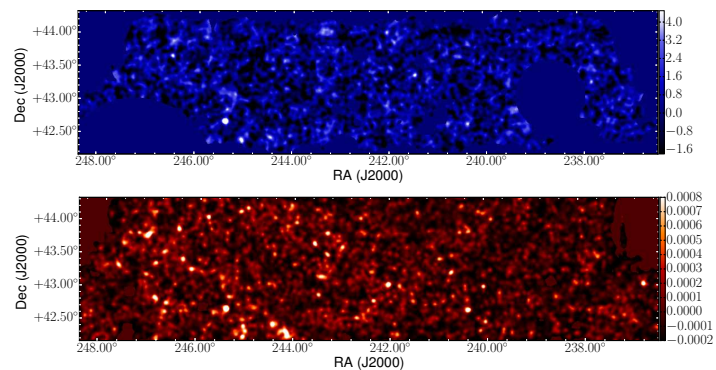


Fig. 7. Same as Figure 3, but for the HECTOMAP field.

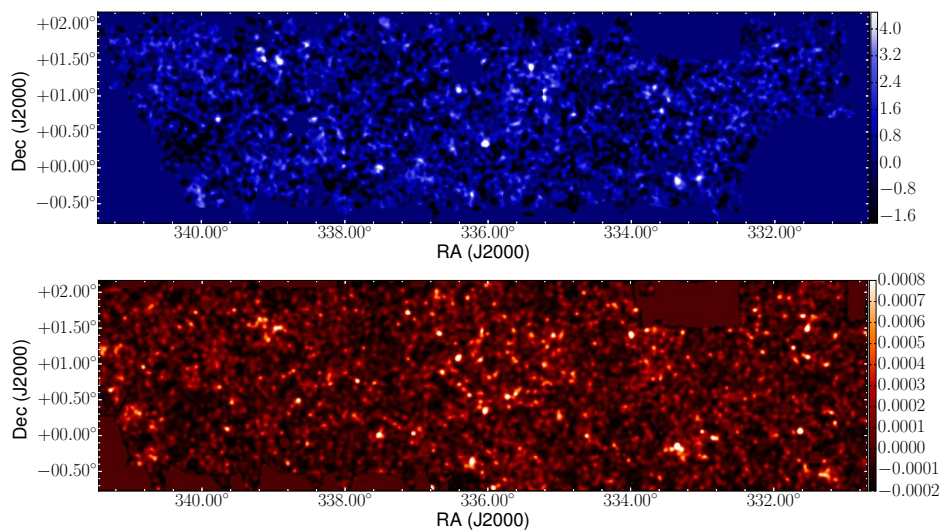


Fig. 8. Same as Figure 3, but for the VVDS field.

### 3.2 Galaxy mass maps

The LRG sample constructed in Section 2.2 is used to create a galaxy mass map, a projected map of stellar masses of LRGs with the same redshift weight as weak lensing. Specifically, we compute a galaxy mass map value in each pixel as

$$\hat{\kappa}_g(\theta_i) = \sum_k \frac{M_{*,k}}{(D(z_k)\Delta\theta)^2\Sigma_{\text{crit}}(z_k)}, \quad (4)$$

where  $k$  runs over LRGs that fall within a pixel centered at  $\theta_i$ ,  $M_{*,k}$  is the stellar mass of  $k$ -th LRG,  $D(z_k)$  is the angular diameter distance to the LRG photometric redshift  $z_k$ , and  $\Delta\theta = 0'.5$  is the size of each pixel. The critical surface density  $\Sigma_{\text{crit}}^{-1}(z_k)$  is computed as

$$\Sigma_{\text{crit}}^{-1}(z_k) = \frac{4\pi G}{c^2} D(z_k) \int_{z_k}^{\infty} dz p(z) \frac{D(z_k, z)}{D(z)}, \quad (5)$$

where  $p(z)$  is the average PDF of photometric redshifts of source galaxies used for the weak lensing analysis, and  $D(z_k, z)$  and  $D(z)$  are angular diameter distances from redshift  $z_k$  to  $z$  and from redshift 0 to  $z$ , respectively. Strictly speaking, the critical surface density has some spatial variation from the large-scale structure of source galaxies, which is not taken in account in the following analysis. From equation (4), we subtract the mean value as  $\hat{\kappa}_g(\theta_i) \rightarrow \hat{\kappa}_g(\theta_i) - \bar{\hat{\kappa}}_g$ , and apply the same Gaussian smoothing kernel (equation 2) as used for the weak lensing mass map to obtain the final galaxy mass map.

We show the galaxy mass maps of the 6 HSC S16A patches in Figures 3, 4, 5, 6, 7, and 8, which are created using the same smoothing scale of  $\theta_s = 2'$  as for the weak lensing mass maps.

### 3.3 Cross-correlations of maps

We quantify the correlation between mass maps from weak lensing and galaxy mass maps from photometric LRGs using the Pearson correlation coefficient. For any two maps  $\kappa_1(\theta_i)$  and  $\kappa_2(\theta_i)$  with zero means,  $\langle \kappa_i \rangle = 0$ , the correlation coefficient  $\rho_{\kappa_1 \kappa_2}$  is defined as

$$\rho_{\kappa_1 \kappa_2} = \frac{\sum_i \kappa_1(\theta_i) \kappa_2(\theta_i)}{[\sum_i \{\kappa_1(\theta_i)\}^2]^{1/2} [\sum_i \{\kappa_2(\theta_i)\}^2]^{1/2}}, \quad (6)$$

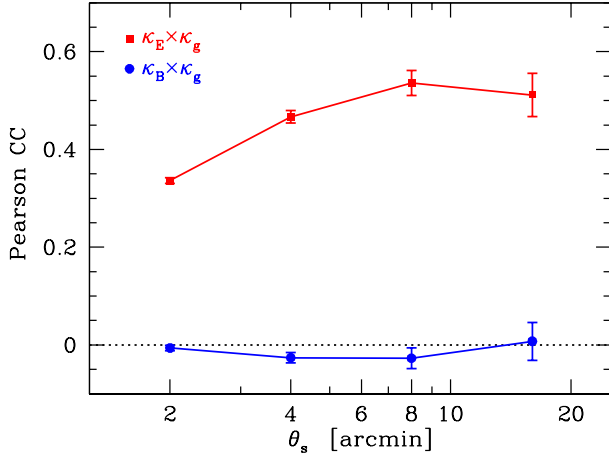
where the summation runs over the pixels. The correlation coefficient becomes  $\rho_{\kappa_1 \kappa_2} \sim 0$  if the two maps are independent, whereas  $\rho_{\kappa_1 \kappa_2} \sim 1$  if the two maps are highly correlated.

We cross-correlate  $E$ -mode and  $B$ -mode mass maps (Section 3.1) with galaxy mass maps (Section 3.2). Since  $E$ -mode mass maps correspond to the true matter distributions, we expect that the galaxy mass maps correlate only with  $E$ -mode mass maps. Figure 9 shows the correlation coefficients as a function of the smoothing size  $\theta_s$  in the Gaussian smoothing kernel. Here we combine the cross-correlation results of all the 6 HSC S16A patches. For each patch, we compute the cross-correlation coefficients and estimate their errors using the 50

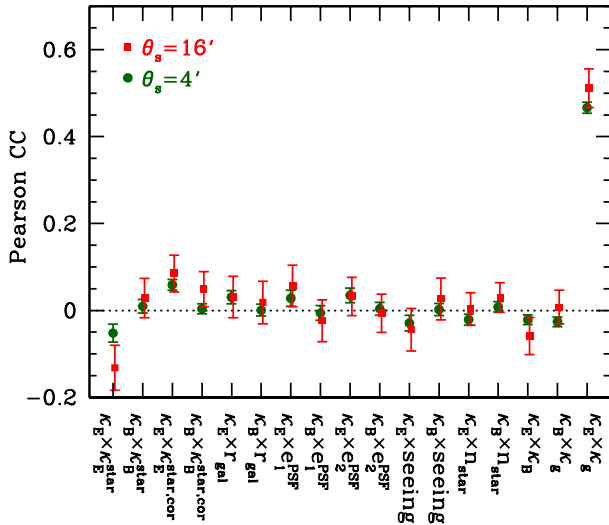
mock samples of the weak lensing shape catalog (Section 2.1). We use the standard deviation of cross-correlation coefficients for the 50 mock samples as our error estimate. We then compute the inverse-variance weighted average of the correlation coefficient of each map combination which we show in Figure 9.

Figure 9 indicates that the  $E$ -mode mass maps indeed correlates well with the galaxy mass maps. The correlation coefficients are consistent with zero for the  $B$ -mode mass maps. We find that the correlation coefficients increase with increasing smoothing size  $\theta_s$ , which is expected because larger smoothing sizes reduce the statistical errors from the shot noise more efficiently. It is worth noting that the HSC mass maps show significant cross correlation ( $\rho = 0.34 \pm 0.01$ ) even for the small smoothing size of  $\theta_s = 2'$ . This result should be compared with previous wide-field mass maps constructed in CFHTLenS (Van Waerbeke et al. 2013) and DES SV (Chang et al. 2015; Vikram et al. 2015) for which much larger smoothing sizes of  $\theta_s \sim 7'$  are required to obtain  $\rho \sim 0.3^1$ . This difference is mainly due to the high density of the shape catalog for weak lensing measurements in the HSC survey. Our study demonstrates that the HSC survey can generate mass maps at higher resolution than CFHTLenS and DES SV, which is crucial for the construction of a mass-selected cluster sample from weak lensing mass maps (Miyazaki et al. 2017b).

Larger correlation coefficients with increasing smoothing scale is understood as follows. The shot noise depends on the source number density  $\bar{n}$  and smoothing scale as  $\sigma \propto (\bar{n}\theta_s)^{-1}$ , where in the range of our interest the fluctuation of a smoothed mass map due to the large-scale structure roughly scales as  $\sigma_{\text{LSS}} \propto \theta_s^{-0.4}$ . Therefore at large  $\theta_s$  the shot noise becomes smaller than  $\sigma_{\text{LSS}}$  that produces a correlation between mass map and galaxy mass maps. This also suggests that the transition smoothing scale beyond which we see large correlation coefficients is inversely proportional to the source number density, which explains the difference between our results and previous results from CFHTLenS and DES SV. However, our result as well as previous results show that correlation coefficients do not approach to unity but saturate at  $\sim 0.5 - 0.6$  at very large  $\theta_s$ , which is presumably due to the combination of several effects, including the limited redshift and mass ranges of the LRG sample, errors in the stellar mass and photometric redshift estimates, and the lack of blue galaxies in the galaxy sample. Intrinsic alignments may also affect our weak lensing mass maps, although the effect of intrinsic alignments on the correlation coefficients is expected to be relatively minor.



**Fig. 9.** Pearson correlation coefficients (equation 6) between mass maps from weak lensing and galaxy mass maps from LRGs as a function of the smoothing size  $\theta_s$  in equation (2). Filled squares show cross-correlations between the  $E$ -mode mass map ( $\kappa_E$ ) and the galaxy mass map ( $\kappa_g$ ). Filled circles show the cross-correlation between the  $B$ -mode mass map ( $\kappa_B$ ) and the galaxy mass map ( $\kappa_g$ ). Errors are estimated from 50 mock samples of the weak lensing shear catalog, which include cosmic variance (see Appendix 1).



**Fig. 10.** Test of systematic effects in weak lensing mass maps from cross-correlations of mass maps with various quantities that are potentially a source of systematics (see also Vikram et al. 2015). We show results for smoothing sizes of both  $\theta_s = 4'$  (filled circles) and  $16'$  (filled squares). For comparison, the rightmost points show the cross-correlation coefficients between weak lensing and galaxy mass maps presented in Figure 9, which represents the physical cross correlation rather than the systematic test. Errors are estimated from 50 mock samples of the weak lensing shear catalog, which include cosmic variance (see Appendix 1).

### 3.4 Systematics tests

Following Vikram et al. (2015), we also examine cross-correlations between weak lensing mass maps and various maps using parameters that potentially act as a source of systematic effects in generating mass maps. While a number of tests have been performed in Mandelbaum et al. (2017), systematics tests based on the mass maps presented here serve as additional checks for validating the shear catalog.

The main source of systematics in weak lensing measurements comes from the PSF. Imperfect corrections of PSFs in galaxy shape measurements can generate artificial correlations between  $E$ - and  $B$ -mode mass maps and PSF parameters. We construct star mass maps  $\kappa_E^{\text{star}}$  and  $\kappa_B^{\text{star}}$  which use star ellipticities  $e_1^{\text{star}}$  and  $e_2^{\text{star}}$  to construct weak lensing mass maps with the same method as described in Section 3.1. The star catalog used for this analysis is the same as the one used for various systematics tests in Mandelbaum et al. (2017). For this purpose, we use both the original star ellipticities  $e_i^{\text{star}}$  as well as star ellipticities after the PSF correction is applied, i.e.,  $e_i^{\text{star,cor}} = e_i^{\text{star}} - e_i^{\text{PSF}}$ . We also create maps of star ellipticities  $e_1$  and  $e_2$  themselves. These maps are constructed first by deriving their average values in each pixel and convolve the maps of these average values with the Gaussian smoothing kernel of equation (2).

In addition, we create maps of seeing sizes, star densities  $n_{\text{star}}$ , and average galaxy sizes of the shape catalog  $r_{\text{gal}}$ , as these parameters may also produce systematic effects in weak lensing shape measurements. Again, these maps are smoothed with the same smoothing kernel.

Figure 10 shows the results for smoothing sizes of both  $\theta_s = 4'$  and  $16'$ . Again, results for all the 6 HSC S16A patches are combined. We find that cross-correlations between weak lensing mass maps and the parameters considered above are small. All the cross-correlations are consistent with zero within  $\sim 2\sigma$  level (given the large number of cross-correlations considered here, we naturally expect that some of the points can deviate more than  $1\sigma$  by chance), which is in marked contrast to the cross-correlations between mass maps and galaxy mass maps, which are detected quite significantly. A possible exception is cross-correlations between star weak lensing mass maps and maps with star (PSF) ellipticities, although their cross-correlation coefficients are much smaller than the cross-correlations between mass maps and galaxy mass maps. This small deviation from zero is presumably due to small residual PSF leakage and PSF modeling errors that are also seen in other systematics tests (see Mandelbaum et al. 2017). We conclude that our weak lensing mass maps constructed in the HSC survey are not significantly affected by systematic effects.

<sup>1</sup> Note that the definition of the smoothing sizes in this paper are different from these previous works by a factor of  $\sqrt{2}$ .

## 4 Three-dimensional mass maps

### 4.1 Three-dimensional mass reconstruction

We can also reconstruct three-dimensional mass maps from weak lensing by taking advantage of photometric redshift measurements for source galaxies. We follow Simon et al. (2009) to use a linear algorithm with the Wiener filtering for the three-dimensional mass reconstruction.

First we consider convergence  $\kappa_l$  for the source redshift bin  $l$  at  $z_{l,\min} < z < z_{l,\max}$ . Since the convergence is the projected matter density field, it can be described by a weighted sum of the density fluctuation  $\delta_k$  at redshift  $z_{k,\min} < z < z_{k,\max}$  as

$$\begin{aligned}\kappa_l &\approx \sum_k \left[ \int_{z_{k,\min}}^{z_{k,\max}} dz \frac{\bar{\rho}(z)}{H(z)(1+z)\Sigma_{\text{crit},l}(z)} \right] \delta_k \\ &\equiv \sum_k Q_{lk} \delta_k,\end{aligned}\quad (7)$$

where  $H(z)$  is the Hubble parameter at redshift  $z$  and the critical density  $\Sigma_{\text{crit},l}^{-1}(z)$  for the source redshift bin  $l$  is approximately given by

$$\Sigma_{\text{crit},l}^{-1}(z) \approx \frac{4\pi G}{c^2} D(z) \frac{D(z, \bar{z}_l)}{D(\bar{z}_l)}, \quad (8)$$

with  $\bar{z}_l = (z_{l,\min} + z_{l,\max})/2$ . Given multiple source and lens redshift bins, Equation (7) reduces to a system of linear equations, which can be inverted easily to obtain  $\delta$  from lensing observables. In practice, however, three-dimensional mass reconstruction is very noisy even with the high source galaxy density of the HSC survey, and therefore an additional regularization is essential. Here we adopt the Wiener filtering which efficiently reduces the noise in the Fourier domain (Simon et al. 2009). We assume that the noise is dominated by the shot noise. Then the noise power between the  $l$ -th and  $m$ -th source redshift bins is given by

$$N_{lm} = \delta_{lm} \frac{\sigma_e^2}{\bar{n}_l}, \quad (9)$$

where  $\delta_{lm}$  is the Kronecker delta,  $\sigma_e$  is the root-mean-square of the source galaxy ellipticity, and  $\bar{n}_l$  is the mean number density of source galaxies in the  $l$ -th bin, both of which are directly estimated from the observation. On the other hand, the signal power in the  $k$ -th and  $n$ -th lens redshift bins is given by

$$S_{kn} = \delta_{kn} C_\ell(z_k), \quad (10)$$

$$C_\ell(z_k) = \frac{1}{(\Delta\chi_k)^2} \int_{z_{k,\min}}^{z_{k,\max}} dz \frac{P^m(k = \ell/\chi)}{H(z)\chi^2}, \quad (11)$$

where  $\Delta\chi_k \approx \Delta z_k / H(\bar{z}_k)$ ,  $\Delta z_k = z_{l,\max} - z_{l,\min}$ , and  $P^m(k)$  is the matter power spectrum, which is computed using the halofit model (Smith et al. 2003; Takahashi et al. 2012). The use of this signal power corresponds to the transverse Wiener filter in Simon et al. (2009). Given the expected signal and noise powers, the three-dimensional mass reconstruction with Wiener filtering from the observed (pixelized) shear maps in different

source redshift bins,  $\gamma$ , is expressed as

$$\delta(\ell) = \tilde{W}(\ell) D^*(\ell) [\alpha \mathbf{S}^{-1} + \mathbf{Q}^T \mathbf{N}^{-1} \mathbf{Q}]^{-1} \mathbf{Q}^T \mathbf{N}^{-1} \gamma(\ell), \quad (12)$$

where  $D(\ell) = \ell^2 / \ell^2$  (Kaiser & Squires 1993), and  $\tilde{W}(\ell)$  is the Fourier transform of the Gaussian smoothing kernel (equation 2).

The parameter  $\alpha$  in equation (12) is an important parameter which tunes the strength of the Wiener filtering. The larger value of  $\alpha$  leads to better signal-to-noise ratios, although it also induces a bias in the redshift of the reconstructed matter structure (Simon et al. 2009). We try several different values of  $\alpha$ , and based on the trial result, in this paper we adopt  $\alpha = 0.03$ , which appears to represent a good compromise between the signal-to-noise ratio and small bias in the redshift.

We need a large smoothing to reduce the shot noise in the three-dimensional mass reconstruction. We adopt the pixel size of  $1'$ , and the smoothing size of  $\theta_s = 20'$  throughout this section. We consider the source redshift range of  $0.1 < z < 2.9$  with the bin size of  $\Delta z = 0.1$ , and the lens redshift range of  $0.05 < z < 1.05$  with the bin size of  $\Delta z = 0.1$ .

We show an example of reconstructed three-dimensional mass maps in Figure 11.

### 4.2 Three-dimensional galaxy mass maps

Three-dimensional galaxy mass maps are also constructed from the LRG sample presented in Section 2.2. The stellar mass density of each pixel with the side length of  $1'$  and  $\Delta z = 0.1$  is simply computed as  $\rho_k = \sum_k M_{*,k} / V$ , where  $V$  is the volume of the pixel. We then apply the same Gaussian smoothing kernel as used in the three-dimensional mass reconstruction in Section 4.1. For each redshift slice, we again subtract the mean value.

An example of three-dimensional galaxy mass maps is also shown in Figure 11.

### 4.3 Cross-correlation results

Following Section 3.3, we quantify the correlation between the three-dimensional mass map (Section 4.1) and the three-dimensional galaxy mass map (Section 4.2) using the Pearson correlation coefficient defined in equation (6). We cross-correlate mass maps in the same or different redshift bins. In order to increase the signal-to-noise ratio further, we combine two redshift bins to have 5 redshift slices at  $0.05 < z < 1.05$  with the width  $\Delta z = 0.2$ . Thus, for each  $E$ - or  $B$ -mode mass map, we compute  $5 \times 5 = 25$  correlation coefficients to check whether we successfully recover the three-dimensional matter structure with weak lensing. In the same manner as in the two-dimensional mass maps, we combine results for all the 6 HSC S16A patches.

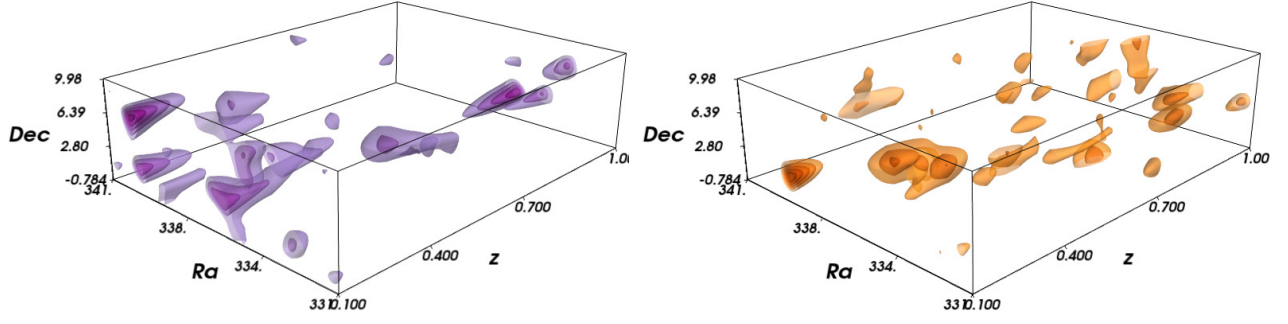


**Fig. 11.** Three-dimensional mass map from the VVDS region (*Left*). We also show the corresponding three-dimensional galaxy mass map from the photometric LRG sample (*Right*). The contours are drawn from  $2\sigma$  to  $6\sigma$  with the  $1\sigma$  interval, where  $\sigma$  is the rms map value.

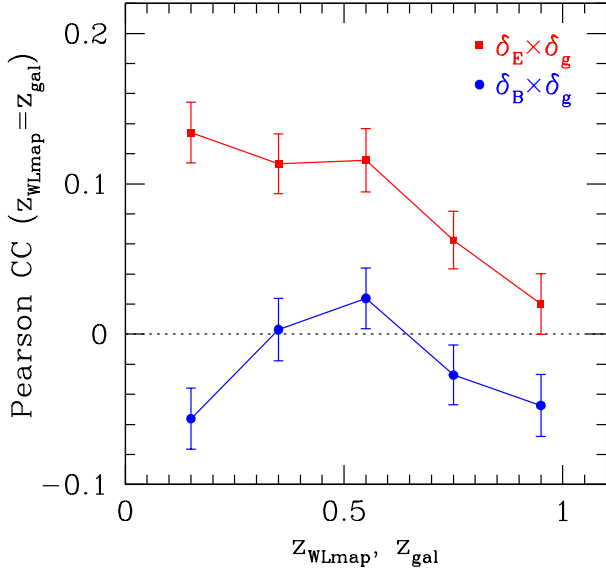


**Fig. 12.** Pearson correlation coefficients (equation 6) between the three-dimensional mass maps from weak lensing and three-dimensional galaxy mass maps from LRGs. Here we show the diagonal correlation coefficients (i.e., same redshift bins for mass maps and galaxy mass maps) as a function of redshift. Both *E*-mode (filled squares) and *B*-mode (filled circles) mass map results are shown. Errors are estimated from 50 mock samples of the weak lensing shear catalog.

Figure 12 shows the diagonal part of the correlation coefficients. We find that the cross-correlations are significantly detected particularly at low redshifts,  $z \lesssim 0.6$ , which indicates the successful three-dimensional mass reconstruction. The correlation coefficients are not very large due to the large effect of the shot noise in three-dimensional mass reconstruction. Although the *E*-mode correlation coefficients decrease at higher redshifts, we find that this is partly due to the redshift bias in reconstructed mass maps. This is obvious from Figure 13, which shows the full correlation matrix of the three-dimensional mass maps and three-dimensional galaxy mass maps. The Figure indicates that the three-dimensional mass reconstruction is indeed successful, but the redshift of the reconstructed mass distribution is biased low particularly at high redshift. As discussed in Section 4.1,

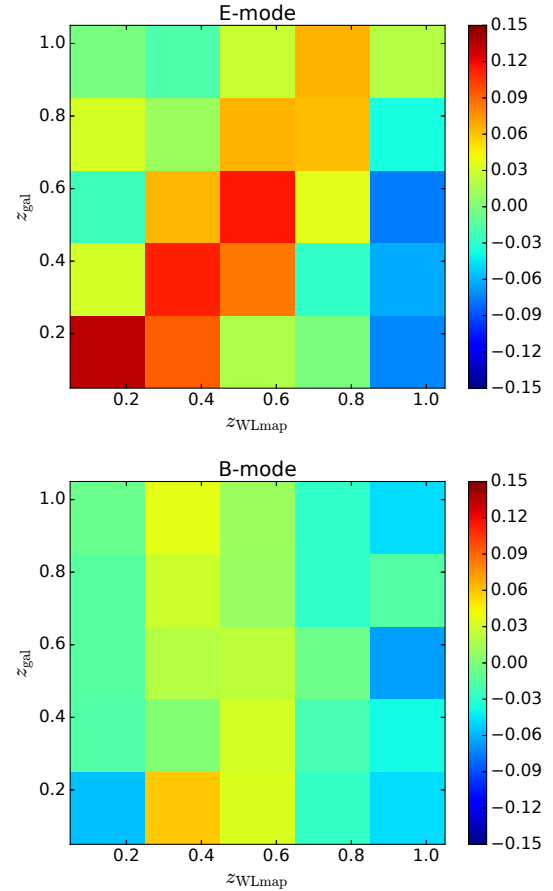


**Fig. 13.** Matrix of Pearson correlation coefficients for the same and different redshift bins between three-dimensional *E*-mode (*upper*) and *B*-mode (*lower*) mass maps and three-dimensional galaxy mass maps. The typical statistical error on the correlation coefficient is  $\sim 0.02$ .

this is in fact expected in our mass reconstruction method because the Wiener filtering method used here is a biased estimator. The redshift bias of  $\Delta z \sim 0.2$  at  $z \sim 0.9$  for our choice of the parameter  $\alpha = 0.03$  is in good agreement with the expected bias estimated by Simon et al. (2009). Since the bias is understood fairly well, in principle we can construct the galaxy mass map with the expected redshift bias of the Wiener filtering method to make a fairer comparison, which we leave for future work. Thus we conclude that we successfully reconstructed three-dimensional mass map out to high redshift, which is made possible thanks to the high number density of the weak lensing shape catalog in the HSC survey.

## 5 Summary

We have presented weak lensing mass maps from the HSC S16A dataset covering  $167 \text{ deg}^2$ . We have cross-correlated projected two-dimensional mass maps with two-dimensional galaxy mass maps constructed from stellar masses of photometric LRGs that are also selected from the HSC data. We have found that the  $E$ -mode mass maps correlate with the galaxy mass maps significantly, even with relatively small smoothing sizes of  $\theta_s = 2'$ . More specifically, the cross-correlation coefficients are  $\rho = 0.54 \pm 0.03$  for  $\theta_s = 8'$  and  $\rho = 0.34 \pm 0.01$  for  $\theta_s = 2'$ . This finding confirms the validity of our weak lensing measurements and weak lensing mass reconstructions. We have also checked for potential systematic effects in mass maps by cross-correlating the weak lensing mass maps with maps of various parameters that can be a source of systematic effects in mass maps, and found that the cross-correlations are sufficiently small. Finally, we reconstructed three-dimensional mass maps from weak lensing using photometric redshift measurements of individual source galaxies. We have found that the three-dimensional mass map correlates reasonably well with three-dimensional galaxy mass map, which indicates that our three-dimensional weak lensing mass reconstruction is successful.

Our work demonstrates the power of the HSC survey for weak lensing studies. This is mainly due to the high number density of source galaxies of  $\bar{n} \sim 25 \text{ arcmin}^{-2}$  for weak lensing analysis. In particular, previous three-dimensional weak lensing mass reconstructions have been limited to relatively small areas (e.g., Massey et al. 2007), and this work successfully applied the technique to much wider area to obtain wide-field three-dimensional mass maps. Given the validation of mass maps presented in this paper, we plan to use HSC weak lensing mass maps to study the large-scale structure of dark matter and baryons, including the construction of a mass-selected cluster sample (Miyazaki et al. 2017b) and the correlation of dark matter and hot gas from the cross-correlation of weak lensing mass maps and Sunyaev-Zel'dovich maps (Osato et al. 2017).

## Acknowledgments

We thank T. Hamana and K. Osato for useful discussions, and the anonymous referee for useful comments. This work was supported in part by World Premier International Research Center Initiative (WPI Initiative), MEXT, Japan, and JSPS KAKENHI Grant Number 26800093, 15H05887, 15H05892, and 15H05893. MO acknowledges financial support from JST CREST Grant Number JPMJCR1414. RM is supported by the US Department of Energy Early Career Award Program. HM is supported by the Jet Propulsion Laboratory, California Institute of Technology, under a contract with the National Aeronautics and Space Administration.

The Hyper Suprime-Cam (HSC) collaboration includes the astronomical communities of Japan and Taiwan, and Princeton University. The HSC instrumentation and software were developed by the National Astronomical Observatory of Japan (NAOJ), the Kavli Institute for the Physics and Mathematics of the Universe (Kavli IPMU), the University of Tokyo, the High Energy Accelerator Research Organization (KEK), the Academia Sinica Institute for Astronomy and Astrophysics in Taiwan (ASIAA), and Princeton University. Funding was contributed by the FIRST program from Japanese Cabinet Office, the Ministry of Education, Culture, Sports, Science and Technology (MEXT), the Japan Society for the Promotion of Science (JSPS), Japan Science and Technology Agency (JST), the Toray Science Foundation, NAOJ, Kavli IPMU, KEK, ASIAA, and Princeton University.

The Pan-STARRS1 Surveys (PS1) have been made possible through contributions of the Institute for Astronomy, the University of Hawaii, the Pan-STARRS Project Office, the Max-Planck Society and its participating institutes, the Max Planck Institute for Astronomy, Heidelberg and the Max Planck Institute for Extraterrestrial Physics, Garching, The Johns Hopkins University, Durham University, the University of Edinburgh, Queen's University Belfast, the Harvard-Smithsonian Center for Astrophysics, the Las Cumbres Observatory Global Telescope Network Incorporated, the National Central University of Taiwan, the Space Telescope Science Institute, the National Aeronautics and Space Administration under Grant No. NNX08AR22G issued through the Planetary Science Division of the NASA Science Mission Directorate, the National Science Foundation under Grant No. AST-1238877, the University of Maryland, and Eotvos Lorand University (ELTE).

This paper makes use of software developed for the Large Synoptic Survey Telescope. We thank the LSST Project for making their code available as free software at <http://dm.lsst.org>.

Based in part on data collected at the Subaru Telescope and retrieved from the HSC data archive system, which is operated by the Subaru Telescope and Astronomy Data Center at National Astronomical Observatory of Japan.

## Appendix 1. Mock shear catalogs

We construct mock shear catalogs which take full account of the survey geometry, the spatial inhomogeneity, and the redshift distribution of galaxies. We do so by adopting a real shear catalog from the observations and replacing the ellipticities of individual galaxies with mock ellipticity values that include the cosmic shear from ray-tracing simulations.

First we review the relation between the ellipticity and the shear in our shear catalog. In this paper we adopt the re-Gaussianization method (Hirata & Seljak 2003), which uses the second moments of the surface brightness distribution of

the source,  $Q_{ij} \propto \int d\vec{\theta} I(\vec{\theta}) \theta_i \theta_j$ , where  $I(\vec{\theta})$  is the surface brightness distribution and the coordinate origin is set to the center of the source, to define the ellipticity of each galaxy. Specifically, a complex ellipticity is defined as  $\epsilon = (Q_{11} - Q_{22} + 2iQ_{12}) / (Q_{11} + Q_{22})$ . In practice a weight function is included in the measurement of the second moment, which is ignored here just for simplicity. The intrinsic ellipticity  $\epsilon^{\text{int}}$  and the observed ellipticity with a weak lensing effect  $\epsilon^{\text{lens}}$  are related as (e.g., Seitz & Schneider 1995)

$$\epsilon^{\text{lens}} = \frac{\epsilon^{\text{int}} + 2g + g^2 \epsilon^{\text{int},*}}{1 + |g|^2 + 2\text{Re}[g\epsilon^{\text{int},*}]}, \quad (13)$$

where  $g = \gamma / (1 - \kappa)$  is the so-called reduced shear.

In order to construct a mock shear catalog, we adopt the real shear catalog from the HSC observation. In the mock catalog, the coordinates of all the galaxies in the shear catalogs are kept unchanged, but we simply replace the observed ellipticities of the individual galaxies,  $\epsilon^{\text{obs}}$ , with simulated values. To derive simulated ellipticity values, first we randomly rotate each galaxy,  $\epsilon^{\text{ran}} = e^{i\phi} \epsilon^{\text{obs}}$ , where  $\phi$  is a random number between 0 and  $2\pi$ . We need to distinguish the intrinsic ellipticity from the measurement error because they have different impacts on the shear responsivity. For each galaxy, the shear catalog has an estimate of the intrinsic rms ellipticity  $\sigma_{\text{int}}$  (parameter `ishape_hsm_regauss_derived_rms_e`) and the measurement error  $\sigma_{\text{sta}}$  (parameter `ishape_hsm_regauss_derived_sigma_e`). For each galaxy, we derive a randomized intrinsic ellipticity as

$$\epsilon^{\text{int}} = f \epsilon^{\text{ran}}, \quad (14)$$

$$f = \frac{\sigma_{\text{int}}}{\sqrt{\sigma_{\text{int}}^2 + \sigma_{\text{sta}}^2}}. \quad (15)$$

We then add weak lensing effects via equation (13) to convert  $\epsilon^{\text{int}}$  to lensed galaxy ellipticity  $\epsilon^{\text{lens}}$ . For weak lensing, we take all-sky weak lensing maps presented in Takahashi et al. (2017). The cosmological model is from the best-fit result of the Wilkinson Microwave Anisotropy Probe nine year data (Hinshaw et al. 2013) with  $\Omega_M = 0.279$ ,  $\Omega_b = 0.046$ ,  $\Omega_\Lambda = 0.721$ ,  $h = 0.7$ ,  $n_s = 0.97$ , and  $\sigma_8 = 0.82$ . Takahashi et al. (2017) created all-sky weak lensing maps at 38 source redshift slices from  $z = 0.05$  to  $5.3$ , which are stored in a HEALPix format (Górski et al. 2005). Although there are realizations with different angular resolutions, we use a low resolution version with NSIDE equal to 4096, which roughly corresponds to a pixel size of  $\sim 1$  arcmin. For each galaxy, we randomly assign its redshift following the photometric redshift PDF of that galaxy (see Tanaka et al. 2017), and obtain values of convergence  $\kappa$  and complex shear  $\gamma$  from the all-sky weak lensing maps at two adjacent redshift slices and linearly interpolating map values. The value of  $\gamma$  is rescaled by a factor of  $(1 + m)$  for each galaxy in order to account for the multiplicative bias (see Mandelbaum et al. 2017). After adding weak lensing ef-

fects from the all-sky ray-tracing simulations, we add a random measurement noise,  $\epsilon^{\text{mock}} = \epsilon^{\text{lens}} + (N_1 + iN_2)$ , where  $N_i$  is a random value drawn from a normal distribution with a standard deviation of  $\sigma_{\text{sta}}$ . From this procedure we create a list of mock ellipticities  $\epsilon^{\text{mock}}$  for the weak lensing shear catalog, which properly include the effect of the cosmic shear. When generating different realizations, we randomly rotate the all-sky weak lensing map before assigning weak lensing effects to randomized galaxies so that we take the different realization of the cosmic shear from the different patch of the all-sky weak lensing map.

## References

- Aihara, H., et al. 2017a, arXiv:1702.08449
- Aihara, H., et al. 2017b, arXiv:1704.05858
- Amara, A., et al. 2012, MNRAS, 424, 553
- Bacon, D. J., & Taylor, A. N. 2003, MNRAS, 344, 1307
- Bartelmann, M., & Schneider, P. 2001, Phys. Rep., 340, 291
- Bell, E. F., et al. 2004, ApJ, 608, 752
- Böhm V., Hilbert S., Greiner M., Enßlin T. A., 2017, arXiv:1701.01886
- Bruzual, G., & Charlot, S. 2003, MNRAS, 344, 1000
- Chang, C., et al. 2015, Phys. Rev. Lett., 115, 051301
- Chang, C., et al. 2016, MNRAS, 459, 3203
- Górski, K. M., Hivon, E., Banday, A. J., Wandelt, B. D., Hansen, F. K., Reinecke, M., & Bartelmann, M. 2005, ApJ, 622, 759
- Hildebrandt, H., et al. 2016, MNRAS, 463, 635
- Hinshaw, G., et al. 2013, ApJS, 208, 19
- Hirata, C., & Seljak, U. 2003, MNRAS, 343, 459
- Hoekstra, H., & Jain, B. 2008, Annual Review of Nuclear and Particle Science, 58, 99
- Hoekstra, H., van Waerbeke, L., Gladders, M. D., Mellier, Y., & Yee, H. K. C. 2002, ApJ, 577, 604
- Hu, W., & Keeton, C. R. 2002, Phys. Rev. D, 66, 063506
- Jullo, E., et al. 2012, ApJ, 750, 37
- Kaiser, N., & Squires, G. 1993, ApJ, 404, 441
- Kubo, J. M., Khiabani, H., Dell'Antonio, I. P., Wittman, D., & Tyson, J. A. 2009, ApJ, 702, 980
- Kuijken, K., et al. 2015, MNRAS, 454, 3500
- Leonard, A., Lanusse, F., & Starck, J.-L. 2014, MNRAS, 440, 1281
- Liu, X., et al. 2015, MNRAS, 450, 2888
- Mandelbaum, R., et al. 2015, MNRAS, 450, 2963
- Mandelbaum, R., et al. 2017, arXiv:1705.06745
- Massey, R., et al. 2007, Nature, 445, 286
- Miyazaki, S., et al. 2002, ApJL, 580, L97
- Miyazaki, S., Hamana, T., Ellis, R. S., Kashikawa, N., Massey, R. J., Taylor, J., & Refregier, A. 2007, ApJ, 669, 714
- Miyazaki, S., et al. 2015, ApJ, 807, 22
- Miyazaki, S., et al. 2017a, PASJ, submitted
- Miyazaki, S., et al. 2017b, in prep.
- Oguri, M. 2014, MNRAS, 444, 147
- Oguri, M., et al. 2017, PASJ, in press (arXiv:1701.00818)
- Okabe, N., Takada, M., Umetsu, K., Futamase, T., & Smith, G. P. 2010, PASJ, 62, 811
- Osato, K., et al. 2017, in prep.
- Pires, S., Starck, J.-L., Amara, A., Teyssier, R., Réfrégier, A., & Fadili, J. 2009, MNRAS, 395, 1265

- Pujol, A., et al. 2016, MNRAS, 462, 35
- Rozo, E., et al. 2016, MNRAS, 461, 1431
- Salpeter, E. E. 1955, ApJ, 121, 161
- Schmidt, F., & Rozo, E. 2011, ApJ, 735, 119
- Schneider, P. 1996, MNRAS, 283, 837
- Seitz, C., & Schneider, P. 1995, A&A, 297, 287
- Shan, H., et al. 2012, ApJ, 748, 56
- Shan, H. Y., et al. 2014, MNRAS, 442, 2534
- Simon, P., Taylor, A. N., & Hartlap, J. 2009, MNRAS, 399, 48
- Simon, P., et al. 2012, MNRAS, 419, 998
- Smith, R. E., et al. 2003, MNRAS, 341, 1311
- Szepietowski, R. M., Bacon, D. J., Dietrich, J. P., Buscha, M., Wechsler, R., & Melchior, P. 2014, MNRAS, 440, 2191
- Takahashi, R., Sato, M., Nishimichi, T., Taruya, A., & Oguri, M. 2012, ApJ, 761, 152
- Takahashi, R., Hamana, T., Shirasaki, M., Namikawa, T., Nishimichi, T., Osato, K., & Shiroyama, K. 2017, arXiv:1706.01472
- Tanaka, M., et al. 2017, arXiv:1704.05988
- Taylor, A. N. 2001, arXiv:astro-ph/0111605
- Taylor, A. N., et al. 2004, MNRAS, 353, 1176
- Utsumi, Y., Miyazaki, S., Geller, M. J., Dell'Antonio, I. P., Oguri, M., Kurtz, M. J., Hamana, T., & Fabricant, D. G. 2014, ApJ, 786, 93
- Utsumi, Y., et al. 2016, ApJ, 833, 156
- VanderPlas, J. T., Connolly, A. J., Jain, B., & Jarvis, M. 2011, ApJ, 727, 118
- VanderPlas, J. T., Connolly, A. J., Jain, B., & Jarvis, M. 2012, ApJ, 744, 180
- Van Waerbeke, L., et al. 2013, MNRAS, 433, 3373
- Vikram, V., et al. 2015, Phys. Rev. D, 92, 022006
- Wittman, D., Dell'Antonio, I. P., Hughes, J. P., Margoniner, V. E., Tyson, J. A., Cohen, J. G., & Norman, D. 2006, ApJ, 643, 128